Systems/Circuits

Distal CA1 Maintains a More Coherent Spatial Representation than Proximal CA1 When Local and Global Cues Conflict

Sachin S. Deshmukh

Centre for Neuroscience, Indian Institute of Science, Bangalore, India 560012

Entorhinal cortical projections show segregation along the transverse axis of CA1, with the medial entorhinal cortex (MEC) sending denser projections to proximal CA1 (pCA1) and the lateral entorhinal cortex (LEC) sending denser projections to distal CA1 (dCA1). Previous studies have reported functional segregation along the transverse axis of CA1 correlated with the functional differences in MEC and LEC. pCA1 shows higher spatial selectivity than dCA1 in these studies. We employ a double rotation protocol, which creates an explicit conflict between the local and the global cues, to understand the differential contributions of these reference frames to the spatial code in pCA1 and dCA1 in male Long–Evans rats. We show that pCA1 and dCA1 respond differently to this local-global cue conflict. pCA1 representation splits as predicted from the strong conflicting inputs it receives from MEC and dCA3. In contrast, dCA1 rotates more in concert with the global cues. In addition, pCA1 and dCA1 display comparable levels of spatial selectivity in this study. This finding differs from the previous studies, perhaps because of richer sensory information available in our behavior arena. Together, these observations indicate that the functional segregation along proximodistal axis of CA1 is not of the amount of spatial selectivity but that of the nature of the different inputs used to create and anchor spatial representations.

Key words: CA1; entorhinal cortex; hippocampus; LEC; MEC

Significance Statement

Subregions of the hippocampus are thought to play different roles in spatial navigation and episodic memory. It was previously thought that the distal part of area CA1 of the hippocampus carries lesser information about space than proximal CA1 (pCA1). We report that distal CA1 (dCA1) spatial representation moves more in concert with the global cues than pCA1 when the local and the global cues conflict. We also show that spatial selectivity is comparable along the proximodistal axis in this experimental protocol. Thus, different parts of the brain receiving differential outputs from pCA1 and dCA1 receive spatial information in different spatial reference frames encoded using different sets of inputs, rather than different amounts of spatial information as thought earlier.

Introduction

The hippocampus is involved in spatial navigation and episodic memory (O'Keefe and Nadel, 1978; Squire et al., 2004). To understand the computations involved in these processes, it is critical to understand information transformation in the entorhinal-

hippocampal network. Cortical information to the hippocampus gets channeled through the medial entorhinal cortex (MEC) and the lateral entorhinal cortex (LEC; Burwell, 2000; Witter and Amaral, 2004). The hippocampus receives path integration derived spatial information from MEC and nonspatial information from LEC (Suzuki et al., 1997; Hafting et al., 2005; Manns and Eichenbaum, 2009; Deshmukh and Knierim, 2011; Knierim et al., 2014), recent studies have demonstrated object dependent allocentric (Deshmukh and Knierim, 2011) and egocentric (Wang et al., 2018) representations of space in LEC. While LEC and MEC Layer II inputs to the dentate gyrus and CA3 are not strongly segregated along the transverse axis of the hippocampus, Layer III inputs to CA1 are. MEC projects preferentially to proximal CA1 (pCA1; close to CA2), while LEC projects preferentially to distal CA1 (dCA1; close to the subiculum; Steward and Scoville, 1976; Naber et al., 2001; Witter and Amaral, 2004). CA3 to CA1 projections
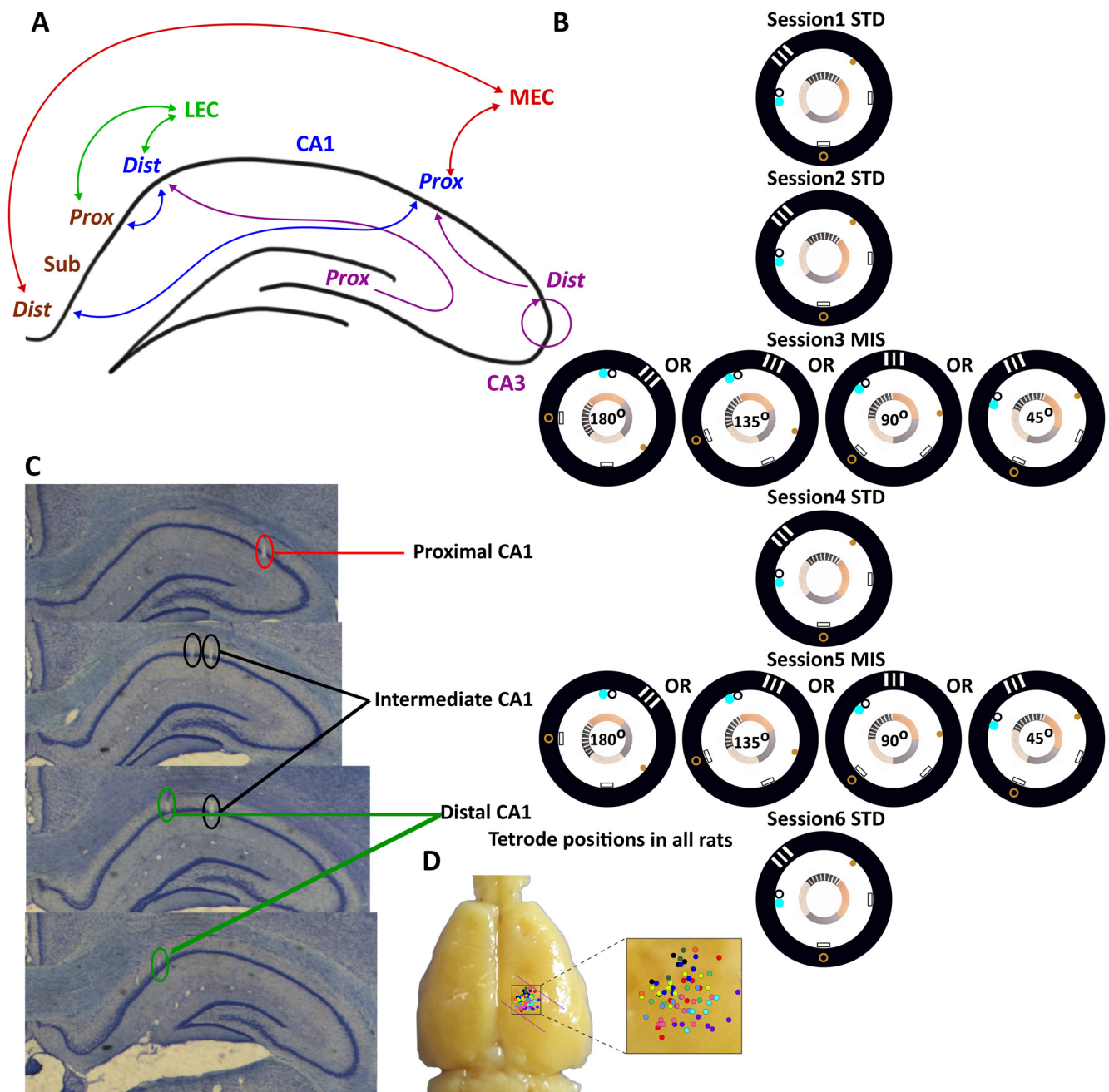
Figure 1. CA1 circuitry and experimental protocol. *A*, Schematic showing anatomic connectivity of CA1 along its transverse axis. Bidirectional arrows indicate reciprocal connections between the two connected areas; unidirectional arrows indicate direction of information flow. *B*, Recording sessions included two mismatch sessions interleaved between standard sessions. All but one rat encountered two standard sessions before manipulations began for a total of six sessions each day, while one rat encountered only one standard session before manipulations began for a total of five sessions each day. Standard sessions had the local as well as the global cues in the configuration the rats were trained on, while mismatch sessions had the local cues rotated CCW and the global cues rotated CW by equal amounts to get a net cue mismatch of 45°, 90°, 135°, or 180°. *C*, Examples of tetrodes recording along the transverse axis of CA1 from one rat. The drive canulae were linearly organized in approximately three rows oriented at 35° to the ML axis to target the entire extent of the transverse axis at the same septotemporal level. *D*, Recording locations in all rats. Tetrodes from a single rat are represented with dots of a single color. Modified with permission from Kumar and Deshmukh (2020).

also show segregation along the transverse axis, with pCA3 projecting preferentially to dCA1 and dCA3 projecting preferentially to pCA1 (Fig. 1A; Ishizuka et al., 1990; Witter and Amaral, 2004).

Correlated with these anatomic differences, CA1 shows functional segregation along its transverse axis. pCA1 has been reported to be spatially more selective than dCA1 (Henriksen et al., 2010; Oliva et al., 2016; Ng et al., 2018). dCA1 neurons

respond to objects and rewards (Burke et al., 2011; Xiao et al., 2020; these studies did not record from pCA1, so we do not know whether pCA1 showed lesser response to objects and rewards). Social place cells, encoding location of a conspecific, are more prevalent in dCA1 than pCA1 of bat (Omer et al., 2018). LEC and dCA1 show enhanced oscillatory synchronization during olfactory-spatial associative memory, while LEC and pCA1 do not (Igarashi et al., 2014). Immediate early gene

expression and lesion studies lend further support to spatial versus nonspatial double dissociation between pCA1 and dCA1 (Ito and Schuman, 2012; Nakamura et al., 2013; Nakazawa et al., 2016). However, the relative contributions of different inputs to the neural representations along the transverse axis of CA1 are not well understood.

A "double rotation" protocol (Shapiro et al., 1997; Knierim, 2002) has been used extensively to study the influence of the local and the global cues on spatial representations in different parts of the hippocampal formation. Individual spatially selective neurons may respond to such manipulations by either rotating with one of the set of cues or by remapping. If neurons in the given region predominantly rotate in concert with either the local or the global cues and the population vector rotates accordingly, the region can be said to respond coherently to the cue manipulation. Along the transverse axis of CA3, pCA3 place cells show an incoherent response while intermediate CA3 (iCA3) and dCA3 place cells show coherent rotation with the local cues (Lee et al., 2015). In the same experimental protocol, MEC shows coherent rotation with the global cues. LEC, which shows very weak spatial tuning during the sessions with the standard cue configuration, shows weak (but statistically significant) rotation with the local cues (Neunuebel et al., 2013). Thus, pCA1 gets strongly coherent but conflicting inputs from MEC (global) and dCA3 (local), while dCA1 gets incoherent inputs from pCA3 and weakly local inputs from LEC. Considering these differences in the entorhinal and CA3 inputs along the transverse axis of CA1, we asked whether pCA1 and dCA1 respond differently to the local-global cue conflict. Our results show that pCA1, which receives strong but conflicting inputs from MEC and dCA3, shows lower coherence in its response to double rotation compared with dCA1. Unexpectedly, spatial selectivity is comparable in this experimental protocol, demonstrating that dCA1 is not necessarily less spatial than pCA1, as claimed in the earlier reports (Henriksen et al., 2010; Oliva et al., 2016; Ng et al., 2018).

Materials and Methods

Subjects and surgery
Eleven male Long–Evans rats aged five to six months were housed individually on a 12/12 h reversed light/dark cycle. All experiments were performed during the night portion of the cycle. Animal care, surgical and euthanasia procedures were in accordance with the National Institutes of Health guidelines and protocols approved by the Institutional Animal Care and Use Committee of the Johns Hopkins University. Custom built hyperdrives with independently moving 15 tetrodes and two references were implanted over the right hemisphere. Rats were implanted with 3D-printed hyperdrives with linearly distributed bundle canulae angled at 35° to the ML axis to target the entire proximodistal extent of CA1 at the same septotemporal level. Data recorded during resting sessions from 8 of these rats was previously used for studying propagation of ripples in CA1 (Kumar and Deshmukh, 2020).

Behavioral training and experimental protocol
Following recovery for about one week after surgery, rats were maintained at 80–90% of their free feeding weight to incentivize them to run on a circular track for food, during the training and the recording sessions. The circular track (56-cm inner diameter, 76-cm outer diameter) had four easily distinguishable sections, and was placed in a room with a 2.75-m diameter circular curtain with 6 large, distinct cues either hanging on the curtain or on the floor along the curtain (Knierim, 2002). Once the rats learned to run in clockwise (CW) direction for food pellets randomly placed on the track, and the electrodes were deemed to be in optimal recording locations, the experimental sessions commenced. Each experimental day had five to six sessions of 15 laps each. The experimental sequence for one rat was STD-MIS-STD-MIS-STD, while that

for all other rats was STD-STD-MIS-STD-MIS-STD. STD stands for standard configuration, and MIS stands for mismatch configuration with one out of the following mismatch angles selected in a pseudorandom order: 45°, 90°, 135°, and 180°. For a given mismatch angle, the local cues on the track were rotated counterclockwise (CCW) by half the amount and the global cues along the curtain were rotated CW by the other half. For example, the local cues were rotated by 22.5° CCW and the global cues were rotated by 22.5° CW for a 45° MIS session (Fig. 1B). These manipulations were performed for 4 d, such that each mismatch angle was sampled twice.

Recording electronics
Neuronal data were collected using an analog wireless transmitter (Triangle Biosystems International). Data from the wireless receiver was processed and stored using cheetah data acquisition system (Neuralynx Inc.). The signals were amplified 1000- to 10,000-fold, bandpass filtered between 600 and 6000 Hz, and digitized at 32,000 Hz for single-unit recordings. Any time one of the channels on a tetrode crossed a preset threshold, data from all four channels on the tetrode were recorded for 1 ms (eight samples before and 24 samples after the threshold). Signals from one of the channels on each of the tetrodes were also amplified 500- to 2000-fold, bandpass filtered between 1 and 475 Hz, digitized at 1 kHz, and stored continuously for local field potential (LFP) recordings.

Data analysis
Unit isolation
Single units were isolated using WinClust, a custom manual cluster cutting software (J. J. Knierim, Johns Hopkins University). For every threshold crossing, waveform characteristics such as peak, valley and energy on all four channels on a tetrode were used for clustering spikes. Only units with fair or better isolation as estimated by cluster separation, waveform and clean interspike interval histogram were included in subsequent analysis. Putative interneurons firing at ≥10-Hz mean firing rate were excluded.

Firing rate maps
Rat's position as well as heading direction were tracked using colored LEDs and a camera recording at 30 frames per second. Off track firing and intervals during which the rats ran slower than 2 cm/s or ran in the wrong direction (CCW) were excluded from the analysis to minimize firing rate variability introduced by non-spatial activity. Linearized rate maps were created at 1° resolution (which gives 360 bins for the circular track) by dividing the number of spikes when the rat was in each bin by the amount of time the rat spent in each bin. Linearized rate maps were smoothed using adaptive binning for computing spatial information scores (bits/spike; Skaggs et al., 1996) and Gaussian filtered ($\sigma = 3$°) for other quantitative analyses. A shuffling procedure was used to determine the probability of obtaining the observed spatial information score by chance. The neuronal spike train was shifted by a random lag (minimum 30 s) with respect to the trajectory of the rat. Spatial information score was computed from the adaptive binned, linearized rate map created from this shifted spike train. This procedure was repeated 1000 times to estimate the chance distribution of spatial information scores and determine the number of randomly time shifted trials having spatial information scores greater than or equal to the observed spatial information scores. Only putative place cells that fired ≥20 spikes, and had statistically significant ($p < 0.01$) spatial information scores of ≥0.5 bits/spike in at least one of the MIS and preceding STD session were used in population vector correlation (PVC) analysis and single-unit responses.

Peak firing rate was the maximum firing rate in the Gaussian smoothed linearized rate map while the mean firing rate was mean of the firing rates in all bins of the same. For the neurons satisfying spatial information criteria and peak firing rates above 1 Hz, place fields were defined as regions with minimum 10 contiguous bins with firing rates above 15% of the peak firing rate or 0.3 Hz, whichever was higher. Number of place fields meeting these criteria in each rate map were counted. Field size was the number of 1° bins in each place field while fraction of track occupied by the place fields was the total number of 1°

bins occupied by all the place fields of a neuron normalized by 360 (total number of bins in the rate map).

Classification of single-unit responses

The angle of rotation giving the highest Pearson correlation between the STD and MIS sessions was used as an estimate of rotation of the neuron's place field. We categorized responses of putative place cells as "appear" (<20 spikes in STD but >20 spikes in MIS), "disappear" (<20 spikes in MIS but >20 spikes in STD), "local" (highest Pearson correlation between STD and MIS after CCW rotation), "global" (highest Pearson correlation between STD and MIS after CW rotation), or "ambiguous" (Pearson correlation coefficient between STD and MIS not crossing a threshold of 0.6 after rotation, or the neuron not meeting the spatial information criteria in one of the sessions). The spike threshold was set rather low, at 20 spikes (Neunuebel et al., 2013; Neunuebel and Knierim, 2014; Lee et al., 2015), to reduce the arbitrariness of neurons being classified as appearing or disappearing. Although this threshold was used for all analyses, using a 50-spike threshold did not substantially alter the results.

PVC analysis

Linearized rate maps were normalized by their peak firing rate before being used for constructing population vectors. Normalized firing rates of all cells for each 1° bin in each MIS or STD session constituted the population vector for that bin for that session. STD versus MIS PVC matrices were constructed by computing Pearson correlation coefficients of the 360 population vectors of each STD and MIS session with each other at all possible relative displacements (0–359°). Similarly, STD versus STD PVC matrices were constructed from STD sessions before and after MIS (Lee et al., 2004). The mean PVC at each relative displacement (0–359°) was computed from each PVC matrix. Peaks [polar (length, angle) pairs converted to cartesian (x,y) pairs], as well as full width at half maximum (FWHM) were estimated from the mean PVC. Normalized bias was defined as the difference between the mean PVCs for all displacements in the direction of the local cue rotation (1–179°) and mean PVCs for all displacements in the direction of the global cue rotation (181–359°) normalized by the mean PVC for all displacements (0–359°).

Shuffle analysis of PVCs

If a given STD versus MIS comparison had n pCA1 and m dCA1 neurons, these $n + m$ neurons were randomly reassigned to shuffled pCA1 and dCA1 groups, with n and m neurons, respectively. Peak PVCs were obtained from the shuffled data as described above. This shuffling procedure was repeated 1000 times to create a peak PVC distribution of the shuffled data.

Bootstrap analysis of PVCs

We performed bootstrap analysis by random sampling with replacement of neurons in the dataset to generate 1000 resampled datasets with the number of samples matching the number of neurons in the actual dataset for each region. Peaks of mean PVCs (x,y), FWHM, and normalized bias were calculated for each of the bootstrap iterations. Because these different parameters have different units and different magnitudes, they were normalized by subtracting their minima and dividing by the difference between their maxima and their minima. This led to all parameters having a range of 0–1. K-means clustering was used to partition the bootstrap distributions from pCA1 and dCA1 into two to four clusters. Principal component analysis (PCA) was used to reduce dimensionality for display purpose.

Statistical analysis

MATLAB (MathWorks) was used to perform statistical analysis. The circular statistics toolbox was used for statistical analysis of circular data. Units were tracked through a recording day, which typically had two MIS sessions with different mismatch angles. Tetrodes with multiple units were left undisturbed from one day to another, while those without units were moved ∼16–32 μm to increase the yield. For tetrodes with units on multiple days, no attempt was made to track units from one

recording day to another. Therefore, while a number of units could be shared between sessions with different mismatch angles, we do not know the exact number of shared units. This partial overlap in number of units violates the assumption of independence made while correcting for multiple comparisons, such as Bonferroni or Holm-Bonferroni correction (Holm, 1979). Thus, rather than using corrections for multiple comparisons, patterns of low p values ($p < 0.05$) across multiple tests were used to draw conclusions. No conclusions were drawn based on single comparisons where multiple comparisons were performed simultaneously.

Histology

On the final day of recording, locations of a small subset of tetrodes were marked by passing 10-μA current for 10 s. Tetrode tracks were reconstructed from coronal sections and confirmed by the marker lesions (Fig. 1C,D; Deshmukh et al., 2010).

Results

Hyperdrives with 15 tetrodes and two references targeting the entire proximodistal extent of dorsal CA1 were implanted on 11 rats to record the activity of putative pyramidal cells as the rats ran CW on a circular track with four distinct textures (local cues) in a circular curtained room with six large global cues along the curtain. Cue manipulation sessions with the global cues moving CW and the local cues moving CCW by equal amounts creating 45°, 90°, 135°, or 180° mismatch (MIS) between the two were interleaved with sessions with cues in their standard configuration (STD; Fig. 1B).

Putative interneurons with mean firing rates >10 Hz (Ranck, 1973; Fox and Ranck, 1981; Frank et al., 2001; Deshmukh and Knierim, 2013) were excluded from analyses. Based on their locations, tetrodes were assigned to equally broad pCA1, intermediate CA1 (iCA1) and dCA1 bands (Henriksen et al., 2010). Nine rats had putative pyramidal neurons recorded from in each of the three bands; one rat had units recorded from pCA1 and iCA1; one rat had units recorded from pCA1 and dCA1. Since iCA1 is expected to have overlapping entorhinal projections (Steward and Scoville, 1976; Naber et al., 2001), although data from all three regions is displayed, quantitative statistical comparisons between regions were limited to pCA1 and dCA1 by prior design.

Properties of single units along the proximodistal axis of CA1

In the first STD session, 156 well-isolated putative pyramidal cells in pCA1 fired at least 20 spikes while the rat was running on the track; 131 neurons in iCA1 and 180 neurons in dCA1 met the same criteria. Mean and peak firing rates in pCA1 and dCA1 were statistically indistinguishable from each other (Wilcoxon rank-sum test, mean firing rate: pCA1 median = 1.24 Hz, dCA1 median = 1.29 Hz, $p = 0.37$; peak firing rate: pCA1 median = 11.97 Hz, dCA1 median = 11.52 Hz, $p = 0.34$). Spatial correlates of neural activity were estimated using a variety of measures. Spatial information scores (Skaggs et al., 1996) in pCA1 and dCA1 neurons were statistically indistinguishable from one another (pCA1 median = 1.92 bits/spike, dCA1 median = 2.11 bits/spike; Wilcoxon rank-sum test, $p = 0.15$). Number of place fields/cell of 139 pCA1 and 140 dCA1 place cells with statistically significant spatial information scores >0.5 bits/spike were similarly indistinguishable (median = 1 for both, Wilcoxon rank-sum test, $p = 0.28$), and so were the fraction of place cells with a single place field (χ^2 test, $p = 0.36$). Furthermore, sizes of 181 pCA1 and 176 dCA1 place fields were statistically indistinguishable (pCA1 median = 44°, dCA1 median = 47°; Wilcoxon
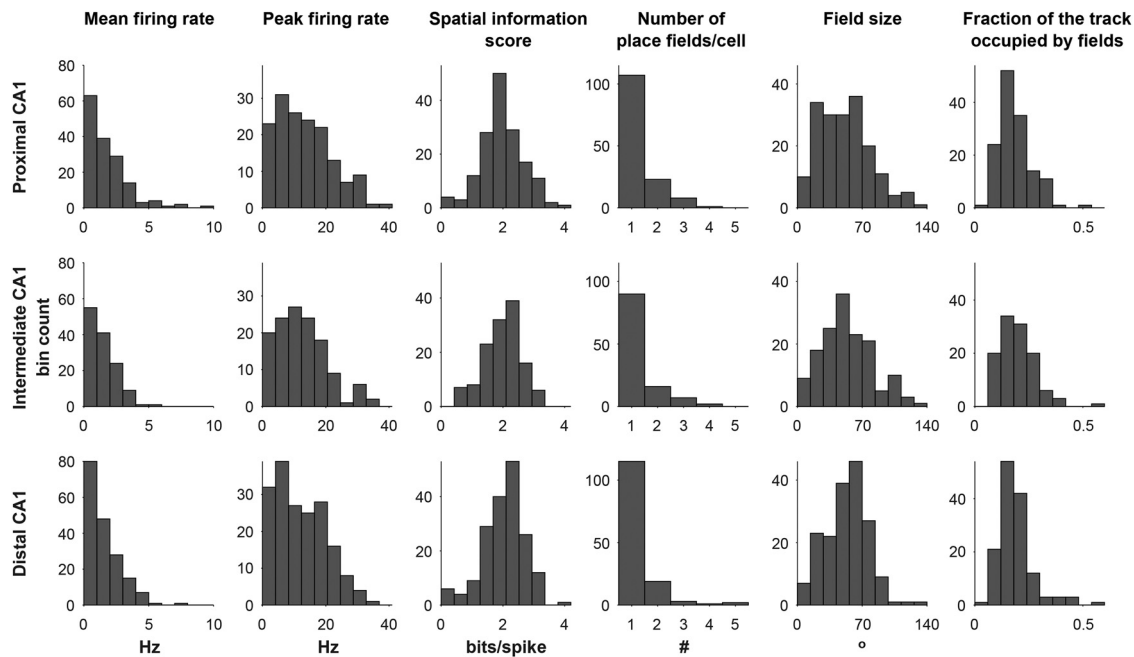
Figure 2. Properties of putative pyramidal cells along the transverse axis of CA1. Mean firing rates, peak firing rates, spatial information scores, number of place fields per cell, place field sizes, and fraction of the track occupied by place fields in pCA1, iCA1, and dCA1 during the first standard session of the day do not differ from one another.

rank-sum test, $p = 0.13$), and so was the fraction of track occupied by all the place fields of pCA1 and dCA1 place cells (pCA1 median = 0.17, dCA1 median = 0.17; Wilcoxon rank-sum test, $p = 0.13$). This lack of difference in spatial correlates of pCA1 and dCA1 (Fig. 2) persisted in MIS sessions regardless of MIS angle. Spatial correlates showed a general decline from STD to MIS session in both regions (Fig. 3).

Single-unit responses to cue manipulation
Responses to cue manipulation of putative place cells (≥ 20 spikes and spatial information score >0.5 bits/spike in at least one of the STD or MIS session) were grouped into five classes (Fig. 4A) as described previously from animals performing the same behavioral task (Lee et al., 2004; Neunuebel et al., 2013). This classification provides a useful qualitative description of single-unit responses that underlie the quantitative differences in populations of neurons across the transverse axis of CA1 discussed in the following sections. However, many neurons are likely to have been recorded in more than one mismatch angle, and classification of neurons into response classes creates arbitrary distinctions. For these two reasons, we did not perform quantitative statistical analysis on the distributions of neurons in these classes, and only present below the classification as qualitative description of response patterns along the transverse axis of CA1.

Using visual inspection, a maximum Pearson correlation coefficient of >0.6 after rotating the rate maps was determined to be a reliable threshold for distinguishing cells that visibly appear to rotate with one set of cues from the cells that respond ambiguously to the cue mismatch (Neunuebel et al., 2013; Neunuebel and Knierim, 2014; Lee et al., 2015). Units that remained spatially selective in both STD and MIS sessions and showed maximum Pearson correlation after rotating the rate maps > 0.6 were classified as rotating neurons, those rotating CW were classified as rotating with the global cues, while those rotating CCW were classified as rotating with the local cues. Units that dropped below the 20 spikes threshold in MIS session

were classified as disappearing units, while those that started firing >20 spikes in MIS after firing less than that in STD were classified as appearing units. Units that failed to meet the maximum Pearson correlation coefficient criterion as well as those which failed the spatial information score criteria in at least one of the sessions while firing >20 spikes in both sessions were classified as being ambiguous. After pooling across all mismatch angles, proportions of appearing, disappearing, and ambiguous units were similar in pCA1 and dCA1, but pCA1 showed more units with CCW rotations in the direction of the local cues while dCA1 showed more units with CW rotations in the direction of the global cues (Fig. 4B). Table 1 shows the distribution of single-unit responses in individual rats. While there is rat to rat variability, seven out of 10 rats with dCA1 units showed more dCA1 neurons rotating with global cues than local cues (the 11th rat did not have any units in dCA1). In contrast, six out of 11 rats showed more pCA1 neurons rotating with local cues than global cues (one rat did not have rotating units in pCA1 but had units that either appeared or disappeared). Furthermore, regardless of whether the majority of neurons rotated with local or global cues, in individual rats, dCA1 often appeared to have a larger fraction of neurons rotating with the preferred cue than pCA1. This observation was confirmed with a statistical comparison using preferred cue indices in individual rats. Preferred cue index for a given region in a given rat was defined as ratio of number of neurons rotating with preferred cues to the total number of rotating neurons. Only rats with at least five rotating neurons in the given region were used in the statistical comparison to minimize extreme indices because of small sample size. Wilcoxon rank-sum test comparing preferred cue indices in dCA1 and pCA1 showed that dCA1 rotated more strongly with preferred cue than pCA1 (pCA1 median = 0.61, dCA1 median = 0.8, $p = 0.046$).

Rotating cells showed clustering of rotation angles near the rotation angles of the local or the global cues in MIS sessions (Fig. 5). These rotation angles were not distributed uniformly in 0–360° range for any of the mismatch angles for any of the CA1
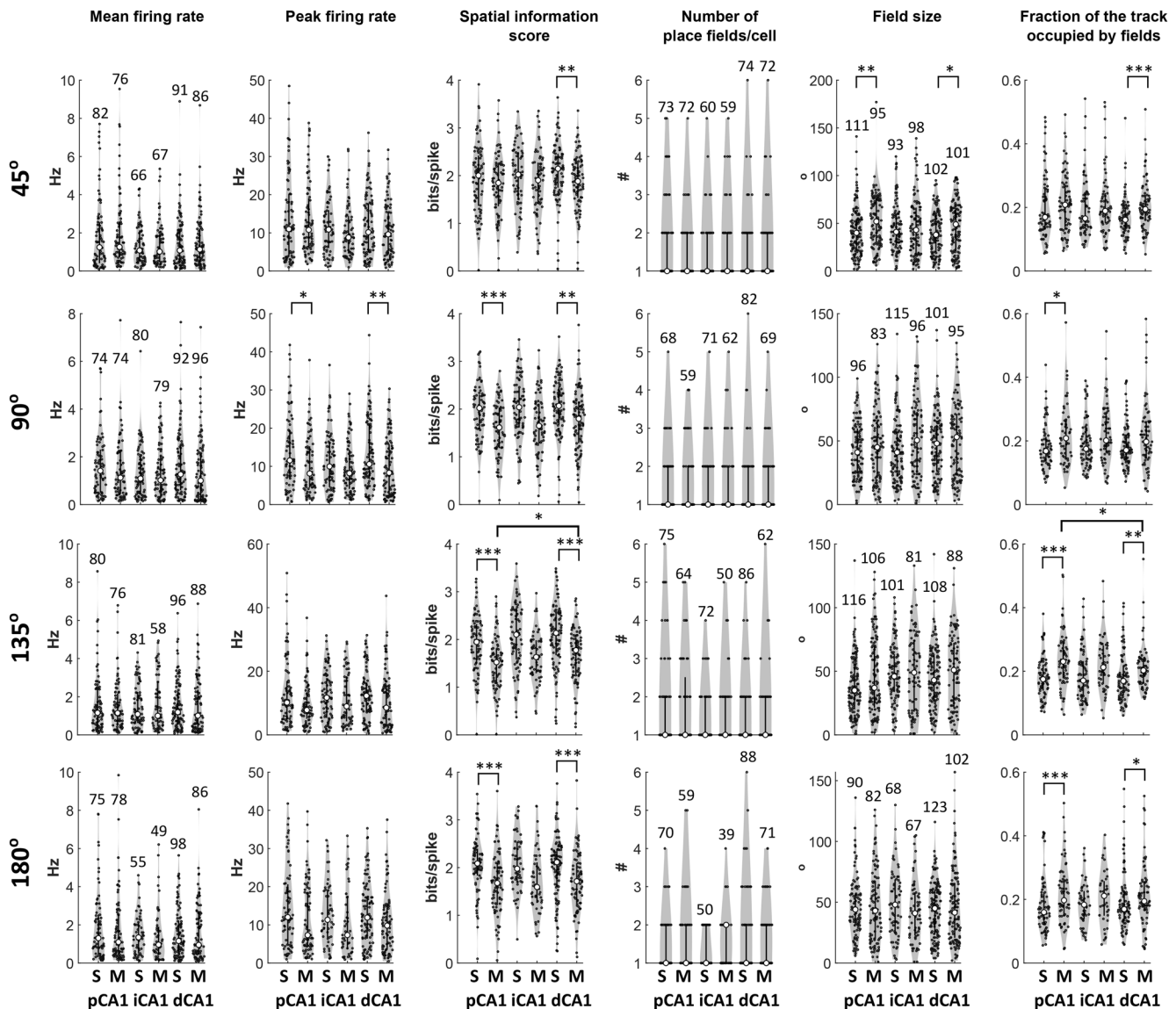
Figure 3. Properties of putative pyramidal cells along the transverse axis of CA1 at all MIS angles. Violin plots (https://github.com/bastibe/Violinplot-Matlab) showing distributions of mean firing rates, peak firing rates, spatial information scores, number of place fields per cell, place field sizes, and fraction of the track occupied by place fields in pCA1, iCA1, and dCA1 for all MIS angles in MIS sessions (M) and the STD sessions preceding them (S). Each black dot represents a neuron for mean firing rates, peak firing rates, and spatial information scores; each black dot represents a place cell for number of place fields per cell and fraction of the track occupied by place fields; each black dot represents a place field for place field sizes. The numbers in mean firing rate plots indicate the numbers of neurons in each group; the numbers in number of place fields per cell plots indicate numbers of place cells in each group; the numbers in field sizes plots indicate the numbers of place fields in each group. White dot indicates the median for each of the plots and the line spans from 25th to 75th percentile. Wilcoxon rank-sum test was performed to compare STD versus MIS sessions for pCA1, STD versus MIS sessions for dCA1, and MIS sessions for pCA1 versus dCA1, for each of the properties being compared here. All significant comparisons are marked in the plots as: *$p < 0.05$, **$p < 0.01$, ***$p < 0.001$. Notice how most of the statistically significant differences are between standard and mismatch sessions of a given region; MIS sessions for pCA1 versus dCA1 showed statistically significant difference only for spatial information score and fraction of the track occupied by place fields for 135° MIS session. In addition, fraction of place cells with one place field per cell was also compared using χ^2 test. None of the STD versus MIS comparisons for pCA1, STD versus MIS comparisons for dCA1, or pCA1 MIS versus dCA1 MIS comparisons were significant at $p < 0.05$.

subregions (Rao's spacing test, $p < 0.001$ for all angles for all regions; pCA1: $n = 58, 41, 48,$ and 35, iCA1 $n = 49, 41, 41,$ and 27, and dCA1: $n = 57, 49, 44,$ and 55 for 45°, 90°, 135°, and 180° MIS, respectively), confirming that they were not distributed by a random process with uniform distribution. Coherence of rotation of the rotating cells was estimated using mean vectors. pCA1 single units showed statistically significant coherent rotations at all mismatch angles (Rayleigh test; MIS 45°: $p < 10^{-5}$; MIS 90°: $p = 0.0009$; MIS 135°: $p = 0.0486$; MIS 180°: $p = 0.0131$). While the mean vectors (Fig. 5A, blue arrows) were rotated CCW toward the local cues for 90°, 135°, and 180°, the mean vector for 45° was rotated CW toward the global cues. In contrast,

mean vectors of dCA1 single units showed CW rotations toward the global cues for all mismatch angles. The mean vectors were statistically significant for all mismatch angles except 180° (Rayleigh test; MIS 45°: $p < 10^{-5}$; MIS 90°: $p < 10^{-5}$; MIS 135°: $p = 0.0268$; MIS 180°: $p = 0.3085$). Mean vector length and Rayleigh test used to measure its significance are flawed when the distribution is clearly bimodal, as seen in Figure 5A. A bimodal distribution gives shorter mean vector lengths, especially when the two modes are 180° apart, even when the distribution is clearly non-random (as confirmed by Rao's spacing test). There was no discernible pattern in the angles of rotation of mean vectors of single units in iCA1, and the mean vectors were
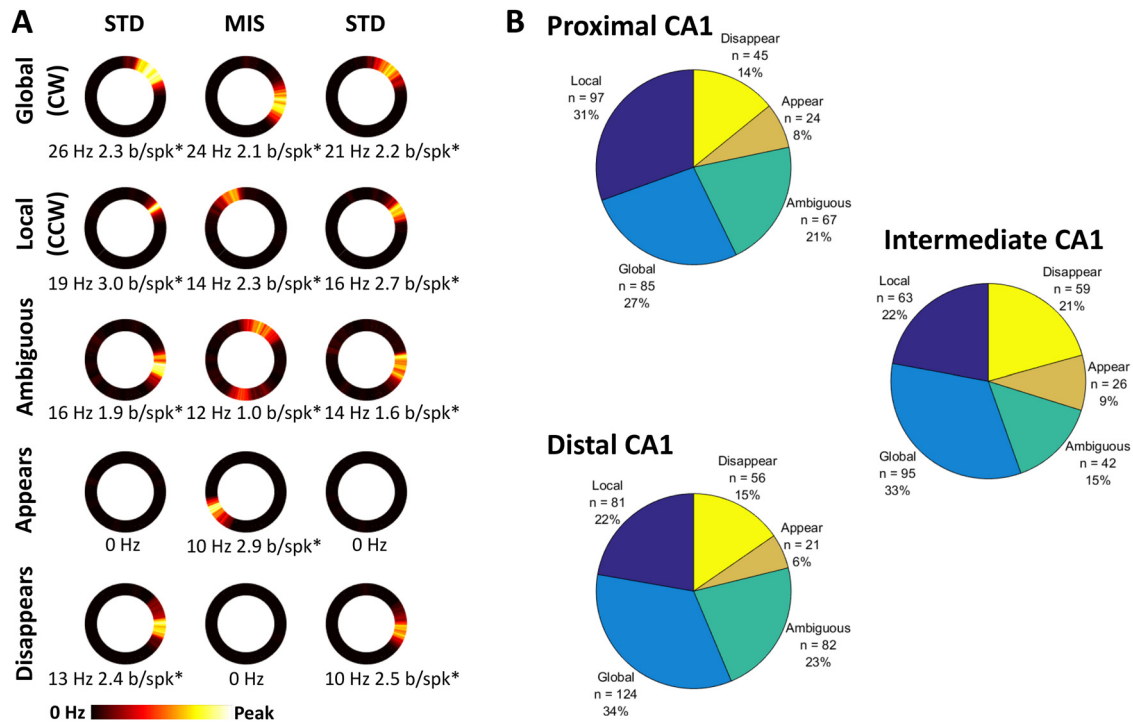
Figure 4. Single-unit responses to cue manipulation. **A**, Examples of units showing different types of responses to cue manipulations. Responses were categorized into five types: CW rotation in the direction of the global cues, CCW rotation in the direction of the local cues, ambiguous rotation, appear in MIS session and disappear in MIS session. Peak firing rates and spatial information scores are shown under each rate map. Asterisks mark statistically significant spatial information scores. **B**, Proportion of different classes of responses in pCA1, iCA1, and dCA1 pooled across the four mismatch angles.

Table 1. Distribution of single-unit responses to double rotation manipulations in individual rats

	Proximal					Intermediate					Distal				
Rat #	L	G	Am	App	Dis	L	G	Am	App	Dis	L	G	Am	App	Dis
245	1	0	0	0	0	7	3	3	2	1	3	11	7	2	6
274	18	20	8	4	9	0	0	0	0	4	0	0	0	0	0
281	3	2	0	1	1	0	0	0	0	0	1	7	4	1	2
302	15	22	17	13	9	21	27	11	3	13	3	2	0	0	2
305	4	2	4	0	1	11	11	8	5	4	22	4	18	2	3
391	12	19	13	1	6	4	10	2	1	15	0	10	8	2	6
392	3	0	1	0	0	5	6	0	0	6	13	6	5	1	4
416	0	0	0	1	2	2	1	1	0	0	2	15	6	1	6
417	32	12	21	2	15	6	9	10	6	8	24	43	21	3	22
432	0	3	0	0	2	2	8	2	2	4	3	13	1	3	2
441	9	5	3	2	0	5	20	5	7	4	10	13	12	6	3
All	97	85	67	24	45	63	95	42	26	59	81	124	82	21	56

Each column shows number of neurons in each rat in each region showing the following responses: L, CCW rotation in the direction of the local cues; G, CW rotation in the direction of the global cues; Am, ambiguous rotation; App, appear in MIS session; and Dis, disappear in MIS session.

statistically significant only at 45°and 90°(Rayleigh test; MIS 45°: $p < 10^{-5}$; MIS 90°: $p < 10^{-5}$; MIS 135°: $p = 0.1331$; MIS 180°: $p = 0.5674$). Across all mismatch angles, pCA1 showed similar proportion of units rotating CW toward the global cues (47%) and CCW toward the local cues (53%). In contrast, both distal and iCA1 showed a preference for CW rotation toward the global cues (60% vs 40% CCW; Fig. 5B).

Population responses to cue manipulation
While the rotating single units in pCA1 and dCA1 demonstrate clear differences, single-unit rotation analysis misses out on contributions of other neurons in the ensemble excluded by the criteria used for classifying single-unit responses to cue

manipulations as rotating. Similarities of population vectors estimated using PVCs (Lee et al., 2004, 2015; Neunuebel et al., 2013) between sessions using all neurons meeting inclusion criteria (statistically significant spatial information scores ≥ 0.5 bits/spike, minimum 20 spikes, mean firing rate < 10 Hz) in either MIS or preceding STD session help overcome this limitation. PVCs between STD sessions preceding and following MIS sessions (labeled STD1 and STD2) were used as control.

Figure 6 shows PVCs for STD1 versus STD2 and STD1 versus MIS for all MIS angles for pCA1, iCA1, and dCA1. The strength of correlation between the population vectors as estimated by Pearson correlation coefficients at all combinations of relative displacements is represented in pseudocolor, with black corresponding to $<= 0$ and white corresponding to 1. If the population representation is unchanged between the two sessions being compared (STD1 vs STD2 or STD1 vs MIS), the population vectors are expected to show highest correlation at 0° displacement from one another. This generates a line of highest correlation at the diagonal going from bottom left to top right of the PVC matrix (black line). If, on the other hand, the population representation coherently rotates between the two sessions being compared, the line of highest correlation (running at 45° angle, parallel to the diagonal) in the PVC matrix is expected to get displaced by the corresponding angle. Colored lines in each PVC matrix show the expected displacement for the given MIS angle for the local (green dashed line) and the global (green continuous line) rotation. STD1 versus STD2 PVC matrices for all MIS angles and CA1 subregions show a strong band of high correlation at the diagonal overlapping with the black line. This indicates that the population representations along the entire extent of CA1 transverse axis remained stable between STD sessions before and after the intervening MIS session regardless of the mismatch angle. In the 45° MIS session, all three regions showed

strong PVC bands, which were slightly displaced toward the green continuous line corresponding to the global cue rotation. In 90°, 135°, and 180° MIS sessions, pCA1 did not show a single coherent band of high correlation parallel to the diagonal. Instead, patches of high correlations were seen overlapping with the local (green dashed line) as well as the global (green continuous line) cue rotations. iCA1 showed a more coherent band of high correlation in the 90° MIS session, which was biased toward the global cue rotation (green continuous line) but showed a patchy distribution of high correlations similar to pCA1 in 135° and 180° MIS. In contrast to these two regions, dCA1 showed a fairly coherent band of high correlation biased toward the global cue rotation (green continuous line) at all mismatch angles with occasional patches of high correlation near the local cue rotations (green dashed line).

Each PVC matrix represents Pearson correlation coefficients between population vectors at each location in STD1 with each location in the session being compared (STD2 or MIS). Thus, the PVC matrix has information about how strongly the population vector at any location in STD1 correlates with population vectors in STD2/MIS at every relative displacement (0−359°). Averaging across locations for a given relative displacement gives a reliable estimate of similarity of population representation at that relative displacement between the two sessions being compared regardless of the location along the track. To obtain this average for all relative displacements, the mean PVC for each relative displacement (0−359°) was calculated from 360 correlation bins along a line running parallel to the bottom left to top right diagonal. Displacement of the line from the diagonal corresponded to the relative displacement between the two sessions (STD1 vs STD2 or STD1 vs MIS). If the population representation remained stable between the two sessions being compared, the mean PVCs are expected to be highest at 0° relative displacement. If, in contrast, the population representation rotated coherently with a set of cues, the mean PVCs are expected to be highest at the corresponding relative displacement.

The mean PVCs (plotted on polar plots below each PVC matrix in Fig. 6) show a narrow distribution with large peaks at or near 0° displacement for STD1 versus STD2 comparisons for all CA1 subregions, as expected when the representations remain stable between sessions being compared. Peaks in the polar plots of all STD1 versus MIS comparisons were smaller than the corresponding STD1 versus STD2 comparisons for all CA1 subregions. For STD1 versus MIS comparison for the 45° mismatch angle, the distribution of mean PVCs widened and showed a bias toward CW rotations (in the direction of the global cue rotation) in all CA1 subregions. As expected from the PVC matrices, the polar plot for higher mismatch angles showed different patterns in different subregions of CA1. pCA1 showed two comparable peaks of substantially reduced magnitude following the local as well as the global cue rotations in the 90° and 135° MIS sessions, and a prominent but small peak rotating CCW (following the local cue rotation) in the 180° MIS session. iCA1 showed peaks rotating CW (following the global cue rotation) in the 90° and 180° MIS sessions, and a two-peaked distribution in the 135° MIS session.
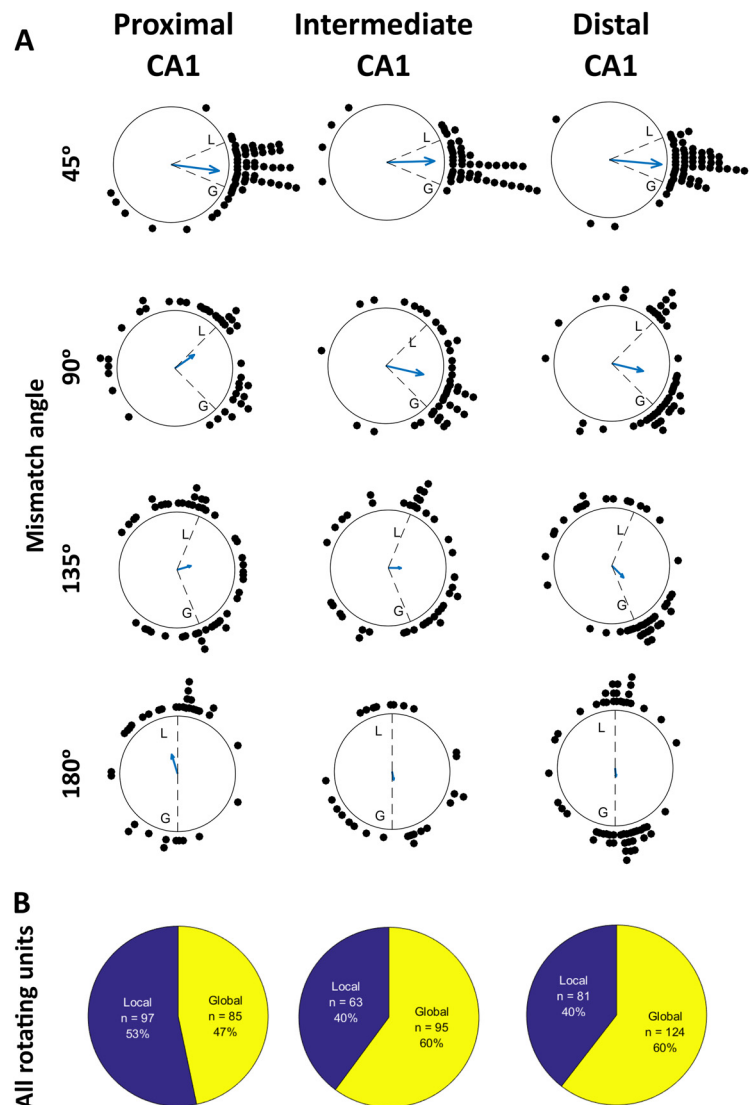

Figure 5. Distribution of single cell rotation angles in response to increasing mismatch angles. ***A***, Angle of rotation of each rotating unit between STD and MIS sessions is represented by a dot around a circle. Mean vector computed from the rotation angles of all units for the given MIS angle is represented by a blue arrow in the center. Angles of rotations of cues between STD and MIS sessions are represented by dotted lines; the local and the global cue rotations are marked by the letters L and G. ***B***, Pie charts showing proportions of rotating units summed across all mismatch angles.

dCA1, in contrast to the other two regions, showed consistent CW rotation with the global cues in the 90°, 135°, and 180° MIS sessions, although substantially smaller peaks corresponding to the local cue rotations could also be seen.

dCA1 showed larger peaks than pCA1 in the polar plots of mean PVCs for STD versus MIS comparisons for all MIS angles, consistent with the visual observation of bands of higher coherence in dCA1 than pCA1 in STD versus MIS PVC matrices. We tested whether these observed patterns of higher peak PVCs in dCA1 than in pCA1 were caused by individual rats by generating STD versus MIS matrices after leaving each individual rat out. All the 11 pairs of PVC matrices for each MIS angle so generated showed higher peak PVCs in dCA1 than pCA1 (Fig. 7A), indicating that none of the rats had disproportionate influence on the peak PVCs leading to the higher peak PVCs observed in dCA1 than pCA1. Orientations of peak PVCs corroborated this observation. All 11 dCA1 peak PVCs for the four MIS angles after dropping each of the rats individually were oriented similar
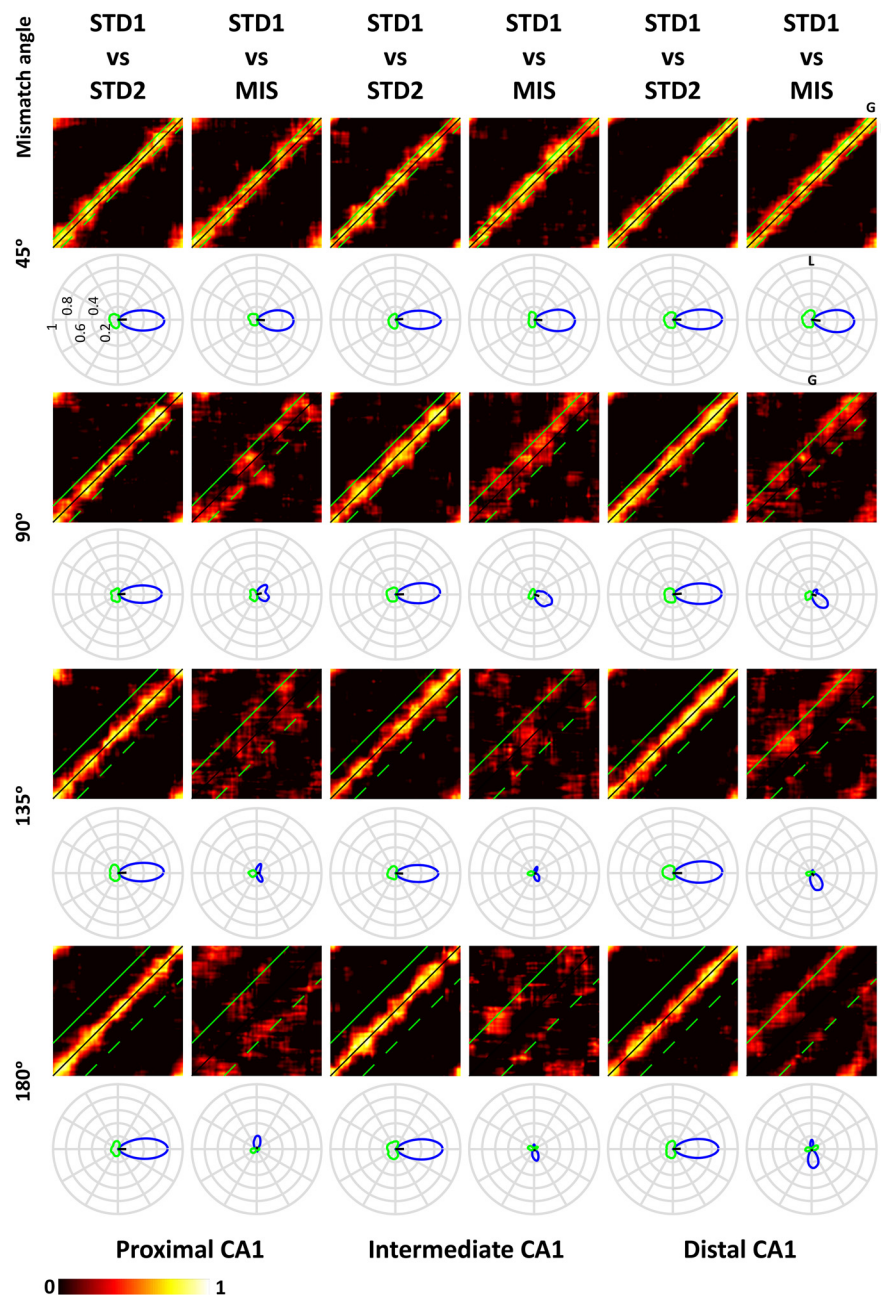
Figure 6. PVCs. PVC matrices for STD1 versus STD2 sessions (STD sessions preceding and following MIS session) and STD1 versus MIS session show magnitude of correlation between population vectors for each 1° position bin on the track as a function of relative displacement between the two sessions being compared. STD1 versus STD2 matrices show a strong band of high correlation around 0° displacement (black line) for all mismatch angles and all subregions of CA1. Red and green lines show the expected displacement of high correlation band corresponding to the local (L) and the global (G) cue rotations in the different mismatch sessions, respectively. STD1 versus MIS matrices show different responses at different mismatch angles for different regions. While dCA1 STD1 versus MIS matrices show a distinct band of high correlation following the global cue rotation (green line) at all mismatch angles, pCA1 and iCA1 STD1 versus MIS matrices show patchy distribution of high correlation at multiple mismatch angles. Polar plots below the PVC matrices show mean of PVCs over all positions at each relative displacement (0−359°). All polar plots had negative correlation coefficients at some orientations. In normal polar plots (which take into consideration both magnitude as well as sign of the correlation coefficients), correlation coefficient of ∼−0.2 at 180° in dCA1 STD versus STD plots would appear as a second line at 0.2 below the actual correlation coefficient of ∼0.8 at 0°, creating a confusing double line. In order to avoid confusion because of the negative correlation coefficients appearing as double lines in the opposite orientations, magnitudes of positive mean correlations are shown in blue while magnitudes of negative mean correlations are shown in green (i.e., 0.2 on green line corresponds to a correlation coefficient of −0.2 at the marked orientation). Black line in the center shows mean vectors computed from the polar plots. Notice the reduced peak correlations at higher mismatch angles for all regions compared with STD1 versus STD2 correlations and STD1 versus MIS correlations at 45°. Contrast the bimodal structure of positive correlations for pCA1 at 90° and 135° with the larger peak following the global cues for dCA1. The outermost circle in the polar plot corresponds to Pearson correlation coefficient of 1 with each concentric circle being spaced at an interval of 0.2.

to the peak PVC for all rats (rotated in direction of the global cues). As expected from the bimodal distribution with two comparable peaks following the local as well as the global cue rotations in the 90° and 135° MIS sessions in pCA1 polar plots (Fig. 6), the peak vector orientation jumped between the two peaks (90° MIS: peak angle after removing seven rats was rotated in the direction of the local cues while that after removing four rats was rotated in the direction of the global cues; 135° MIS: peak angle after removing six rats was rotated in the direction of the local cues while that after removing five rats was rotated in the direction of the global cues; Fig. 7B).

To statistically characterize the PVCs, we performed two complementary statistical analyses using resampling techniques on the pCA1 and dCA1 populations. We performed a shuffle analysis to test whether the pCA1 and dCA1 neurons come from a common neuronal pool. For this analysis, the neurons from both regions were pooled together before being randomly reassigned to pCA1 or dCA1 to generate distributions of pCA1 and dCA1 neurons under simulated condition of both the populations coming from the same common pool. Comparison of the observed pCA1 and dCA1 PVCs with these simulated distributions were used to determine whether either of them rotated more coherently than the common pool. We also performed a bootstrap analysis to compare pCA1 and dCA1 populations directly with each other. For this analysis, a bootstrap distribution of pCA1 neuronal population was generated by sampling with replacement from the pCA1 neurons, and a bootstrap distribution of dCA1 neuronal population was generated by sampling with replacement from the dCA1 neurons.

We performed 1000 shuffles to create shuffled peak PVC distributions for pCA1 and dCA1. A higher peak vector correlation than expected from this distribution indicates that the given region rotates more coherently than the common pool. Figure 8 shows that dCA1 consistently has higher correlation than the 95th percentile of the shuffled distribution across all MIS angles (45°: $p = 0.019$; 90°: $p = 0.026$; 135°: $p = 0.012$; 180°: $p < 0.001$) while pCA1 does not (45°: $p = 0.953$; 90°: $p = 0.938$; 135°: $p = 0.983$; 180°: $p = 0.297$). Thus, dCA1 consistently rotates more coherently than expected under the assumption that pCA1 and dCA1 neurons come from a common pool, while pCA1 does not.
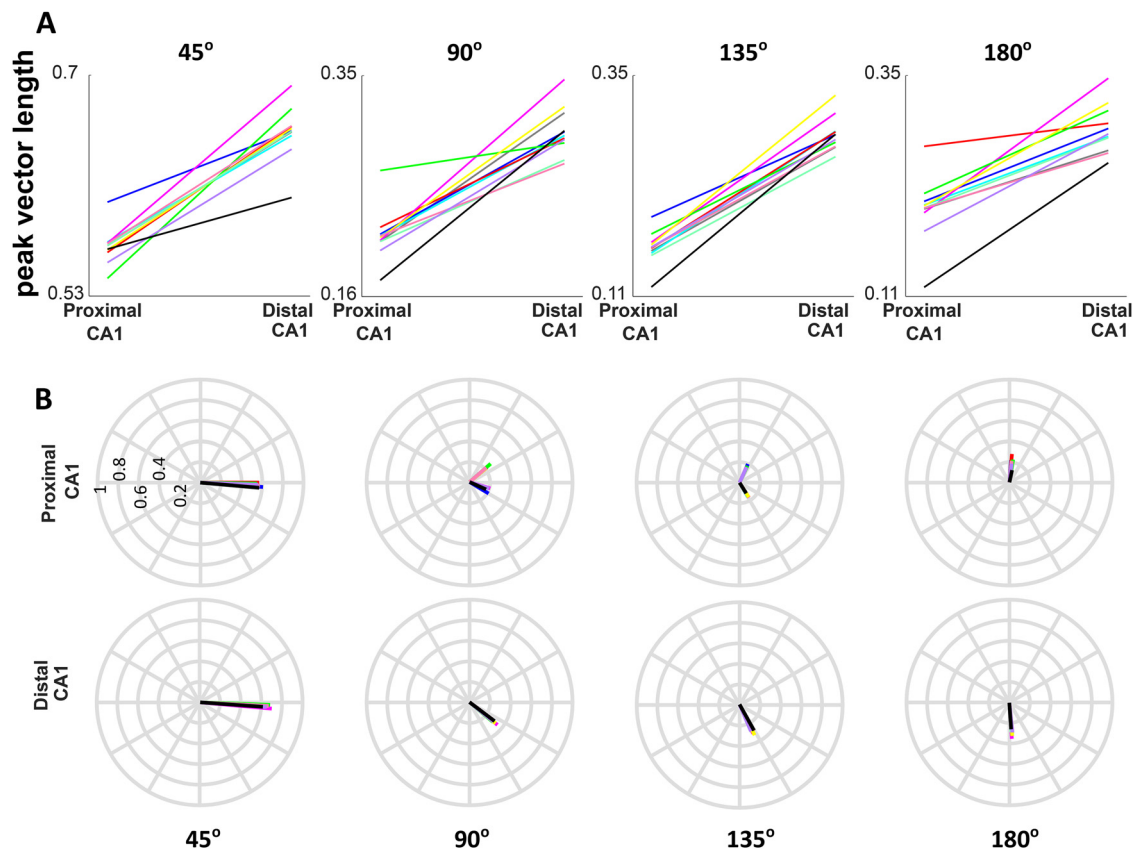
Figure 7. Test for influence of individual rats on peak PVCs. To test whether individual rats disproportionately influence the peaks in the mean PVC polar plots, STD versus MIS PVC matrices were generated after leaving each of the rats out in turn, and polar plots of mean PVCs were constructed followed by measurement of peak PVCs as described earlier. *A*, Each line connects magnitude of peak PVCs in pCA1 with that in dCA1 after removal of all neurons from a particular rat from the dataset. Removal of a particular rat is represented by the same color across all MIS angles, and the color code matches that used in Figure 1. *B*, Polar plots of peak PVCs of pCA1 after removal of individual rats show the angle of the peak PVCs switching between L and G orientations and 90° and 135° MIS, in line with the bimodal distributions seen in Figure 6. In contrast, peak PVCs of dCA1 continue rotating with global cues after removal of individual rats.

To compare pCA1 and dCA1 STD versus MIS PVCs explicitly, repeated sampling with replacement of neurons from each region was performed 1000 times to generate bootstrapped distributions for the two regions. Unlike the previous shuffle analysis, the pCA1 and the dCA1 populations were kept segregated while generating the bootstrapped distributions in this analysis. The number of samples in each iteration matched the number of neurons in the real dataset for each subregion. These bootstraps allow us to estimate sample distribution of the PVC for each region. For each of the iterations, PVC matrices were generated and mean PVC polar plots for each relative displacement were computed from those matrices. The following parameters were estimated from the polar plots to facilitate comparison between pCA1 and dCA1: peak vectors (*x,y* pairs), FWHM, and normalized bias (for definitions of and calculations of these parameters, see Materials and Methods). PCA was performed on this 4D space for reducing dimensionality for display purposes. Figure 9 shows the projection of the bootstrapped data for the two regions on the first two principal components for the different mismatch angles. pCA1 bootstraps are shown in red and dCA1 bootstraps are shown in blue. Three clear patterns stand out in all four plots. First, the two distributions are well segregated along the two principal components, with the first principal component showing a clear segregation between the two at all mismatch angles other than 135°. This segregation indicates that pCA1 and dCA1 mean PVC distributions for STD versus MIS comparison are different from one another. Second, the dCA1 bootstrap distribution is much more compact at all mismatch angles than the

pCA1 bootstrap distribution. This visual observation is supported by the mean distance of all bootstraps from each CA1 subregion from the centroid of the same region. Across all MIS angles, dCA1 mean distance from centroid was shorter than pCA1 mean distance from centroid (mean distance from centroid: 45°: pCA1: 0.238, dCA1: 0.197; 90°: pCA1: 0.317, dCA1: 0.188; 135°: pCA1: 0.449, dCA1: 0.153; 180°: pCA1: 0.197, dCA1: 0.127). Third, the pCA1 bootstrap distribution often shows multiple clusters, while most of the dCA1 bootstraps stay together in a single compact cluster. The multiple modes in the pCA1 distributions indicate that the underlying population has multiple competing rotational propensities of comparable magnitudes in response to cue conflict. In contrast, compact unimodal clusters in the dCA1 bootstrapped distribution indicate that the dCA1 population responds more coherently to cue conflict. This observation corroborates the pattern of responses seen in the PVC matrices in Figure 6.

To test whether these distributions of pCA1 and dCA1 bootstraps are indeed different from one another in an unbiased manner, k-means clustering with k = 2, 3, and 4 was employed. Table 2 shows numbers of points from pCA1 and dCA1 that were included in each of the 2/3/4 clusters. For k = 2, at 135° mismatch, all the dCA1 points and a group of pCA1 points clustered together, while the remaining pCA1 points formed the other cluster. For all other mismatch angles, the clusters include >95% of the points from one region while including <5% of the points from the other region, as expected from Figure 9. For k = 3 and k = 4, >95% of the dCA1 points remained together in a single
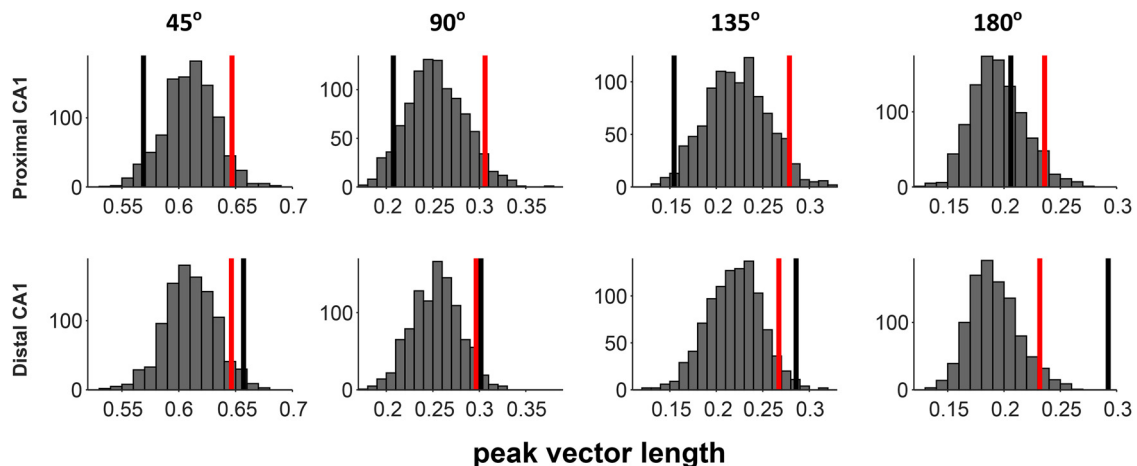
Figure 8. Shuffle analysis for PVCs. Distributions of 1000 PVCs obtained by pooling together neurons from pCA1 and dCA1, and randomly reassigning neurons to pCA1 and dCA1 are shown in each histogram. Vertical black lines mark the PVCs observed in real data, while vertical red lines mark the 95th percentiles of the shuffled distributions. dCA1 has higher PVCs than the 95th percentile of the shuffled distributions for all MIS angles, while pCA1 does not.

cluster for all MIS angles except for k = 4 at 135°, where >90% of the dCA1 points remained together in a single cluster. In contrast, pCA1 points got distributed in multiple clusters for k = 3 and k = 4 for all MIS angles. These clustering patterns prove that pCA1 and dCA1 respond differentially to the double rotation cue manipulation, and that dCA1 population rotates more coherently than the pCA1 population.

Discussion

Dissociation of responses to double rotation manipulation between pCA1 and dCA1

pCA1 and dCA1 are expected to respond differently to local-global cue conflict, given the differential responses of their EC and CA3 inputs. dCA1 does not receive a strong, coherently rotating signal from either CA3 or LEC. pCA3 responds incoherently to double rotation, with sporadic hotspots of high correlation in the PVC matrices of MIS angles >45° (Lee et al., 2015). These sporadic hotspots sometimes rotate with the local cues while rotating with the global cues at some other times. LEC neurons show a weak spatial selectivity on the circular track in STD sessions (Yoganarasimha et al., 2011). Neither the STD1 versus STD2 nor the STD1 versus MIS PVC matrices for LEC show an unambiguous band of high correlation, but polar plots of mean PVCs reveal a weak but statistically significant rotation with the local cues (Neunuebel et al., 2013). LEC encodes external items in egocentric coordinates (Wang et al., 2018). However, the rat typically faces in a certain direction at each position on the circular track, causing the allocentric and the egocentric reference frames to be confounded. Hence, we expect the local cues to weakly dominate over the global cues (Neunuebel et al., 2013) even in the egocentric reference frame.

These weakly local and incoherent inputs from LEC and pCA3 predict either incoherent or weakly local response in dCA1. Surprisingly, dCA1 shows a more coherent rotation than pCA1 in this study, rotating with the global cues at all MIS angles. Alternative sources of spatial information anchored to the global cues may explain these results. In the absence of strong competing inputs, dCA1 may follow the sparse projections from MEC (Masurkar et al., 2017) to rotate with the global cues. Nucleus reuniens sends direct projections to CA1 (Dolleman-Van Der Weel and Witter, 1996; Vertes et al., 2006; Dolleman-van der Weel et al., 2019), and shows head direction (HD) cells

(Jankowski et al., 2014), place cells, and border cells (Jankowski et al., 2015). While nucleus reuniens neurons have not been recorded in the double rotation task, HD cells recorded in other thalamic nuclei (ADN, AVN, LDN, VAN, and RT) rotate with the global cues (Yoganarasimha et al., 2006). HD selectivity reported in CA1 (Leutgeb et al., 2000) and anecdotal observation of HD signal in dCA1 by us as well as others (Buzsáki and Peyrache, 2016; https://www.youtube.com/watch?v=2da6gzF9eo0&t=24m13s) support the hypothesis that HD inputs may be involved in rotation of dCA1 with the global cues. Subiculum, which receives direct projections from the HD system as well as MEC (Ding, 2013), sends feedback projections to CA1 (Xu et al., 2016) and rotates coherently with the global cues in the double rotation task (Sharma et al., 2020). While these inputs from MEC, nucleus reuniens, and the subiculum to dCA1 may be less numerous than LEC and pCA3, they may be strong enough to drive dCA1 to rotate with the global cues in absence of competing strong inputs rotating with the local cues. While the HD system prefers global cues, it is known to occasionally rotate coherently with local cues (Yoganarasimha et al., 2006). This occasional rotation of HD system with local cues, together with statistical noise, could possibly explain the minority of rats showing more neurons rotating with local cues than global cues in dCA1.

In contrast to dCA1, pCA1 gets strong, conflicting inputs from dCA3 (Lee et al., 2015) and MEC (Neunuebel et al., 2013) rotating with the local and the global cues, respectively, during double rotation. Thus, the incoherent response of pCA1 may be explained by differential strengths of CA3 and MEC inputs to individual pCA1 neurons. Neurons with predominant inputs from either CA3 or MEC may follow that input, while those without a clearly dominant input from CA3 and MEC may give ambiguous or remapping responses.

Spatial selectivity in pCA1 and dCA1

In this study, pCA1 and dCA1 show comparable spatial selectivity as estimated using spatial information score, number of place fields per cell, field size, and fraction of the track occupied by fields in STD as well as MIS sessions. This lack of difference in spatial selectivity along the transverse axis contradicts prior studies showing higher spatial selectivity in pCA1 compared with dCA1 (Henriksen et al., 2010; Oliva et al., 2016; Ng et al., 2018).
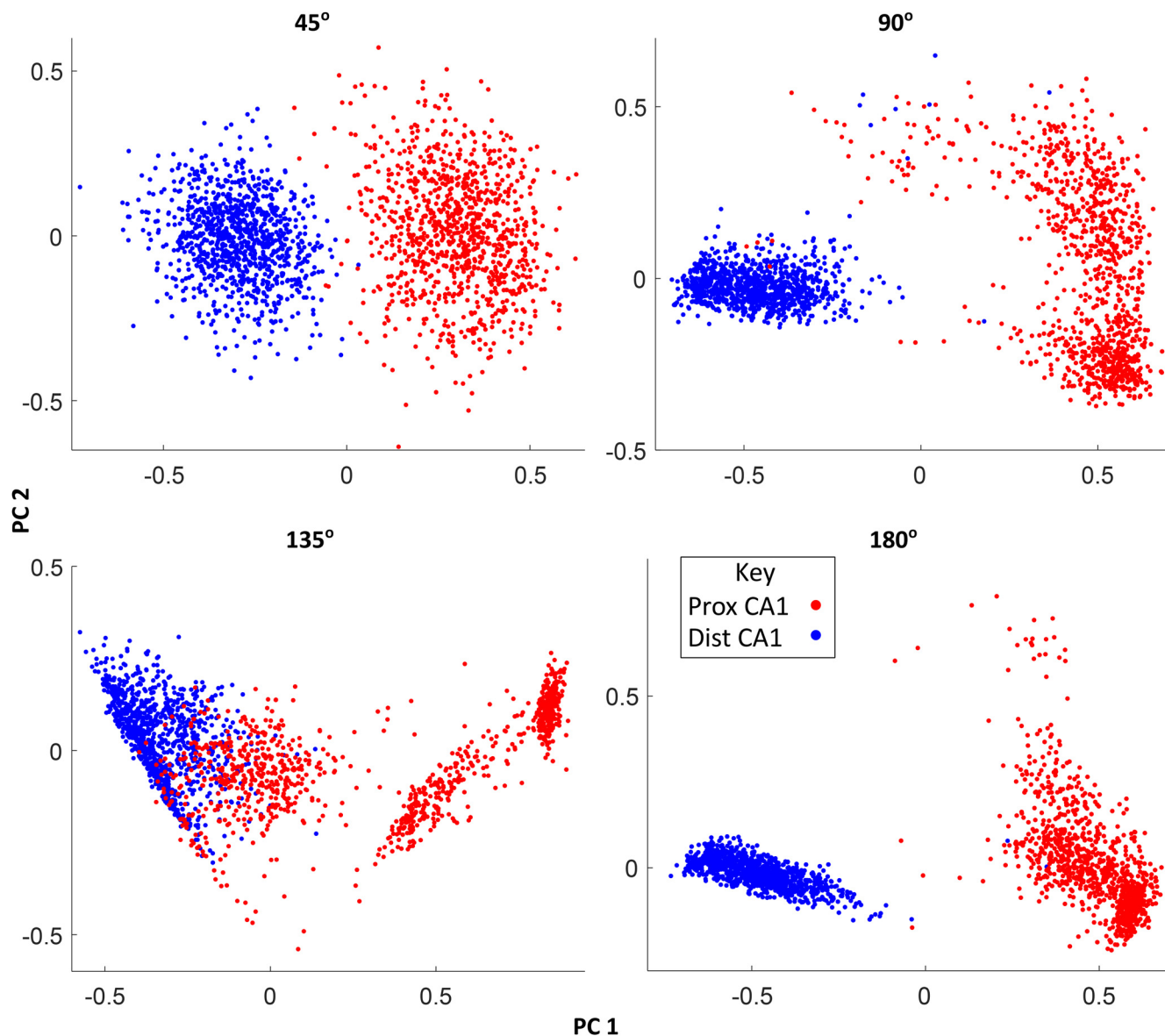
Figure 9. Bootstrap analysis for PVCs. Bootstrapped distributions were created for pCA1 and dCA1 by resampling, with replacement, neurons within each of the two regions 1000 times. Number of samples in each iteration matched the number of neurons in the actual dataset. Peak vectors (*x,y* pairs), FWHM, and normalized bias were measured from the mean PVCs for all iterations. For each mismatch angle, PCA was run on this four-dimensional space, and the first two principal components were plotted to enable visualization of the bootstrapped distribution for pCA1 (red dots) and dCA1 (blue dots). Notice tighter clustering of dCA1 points compared with pCA1 points, which often form multiple clusters.

Table 2. K-means clustering of pCA1 and dCA1 bootstraps with k = 2, k = 3, and k = 4

MIS angle	Region	K = 2		K = 3			K = 4			
		Number of points in cluster 1	Number of points in cluster 2	Number of points in cluster 1	Number of points in cluster 2	Number of points in cluster 3	Number of points in cluster 1	Number of points in cluster 2	Number of points in cluster 3	Number of points in cluster 4
45°	pCA1	**991**	9	481	514	5	404	349	244	3
	dCA1	1	**999**	0	3	**997**	0	0	14	**986**
90°	pCA1	**963**	37	517	464	19	419	498	77	6
	dCA1	4	**996**	1	5	**994**	0	1	11	**988**
135°	pCA1	534	466	309	245	446	310	222	430	38
	dCA1	0	**1000**	0	1	**999**	0	0	92	**908**
180°	pCA1	**995**	5	569	429	2	524	48	426	2
	dCA1	2	**998**	0	2	**998**	0	0	2	**998**

Number of bootstraps from pCA1 and dCA1 in each cluster obtained by k-means clustering with k = 2, k = 3, and k = 4. When >90% of the bootstraps for a given region (pCA1 or dCA1) cluster together, they are shown in bold.

The behavioral arenas used in the earlier studies had a single uniform texture, while the circular track in the present study had four easily discernible sections with distinct textures, visual appearances, and odors. Thus, the apparent elimination of differences in spatial selectivity between pCA1 and dCA1 could possibly be caused by richer sensory information available from the behavioral arena. This study was designed to test how dCA1 and pCA1 respond to local-global cue conflict. This strategy has helped understand the control of different components of the spatial navigation system by local and global cues in a number of hippocampal regions and subregions (Lee et al., 2004, 2015; Yoganarasimha et al., 2011; Neunuebel et al., 2013; Neunuebel and Knierim, 2014; Sharma et al., 2020). To create such a conflict, the local cues on track need to be salient and easy to distinguish, so that they may compete with the prominent global cues along the curtains. However, the increased salience of local cues in this protocol; creates a possible confound. dCA1 may receive stronger inputs because of higher activation of LEC by the textures on the track, which may be thought of as nonspatial, sensory inputs, which just happen to be associated with specific locations on the track. However, LEC shows weak spatial selectivity on the circular track used here, similar to the weak spatial selectivity displayed by LEC in 2D environments with uniform textures (Yoganarasimha et al., 2011; Neunuebel et al., 2013). This weak activation of LEC by sensory inputs from the track is insufficient to account for the apparent increase in spatial selectivity of dCA1 in this protocol. This hypothesis is further bolstered by the observation that dCA1 preferentially rotates with global rather than local cues. Hence, projections from MEC (Masurkar et al., 2017), nucleus reuniens (Dolleman-Van Der Weel and Witter, 1996; Vertes et al., 2006; Dolleman-van der Weel et al., 2019), and the subiculum (Ding, 2013; Xu et al., 2016) to dCA1, discussed earlier, need to be considered. However, these inputs would also have been available to dCA1 in the earlier experiments (Henriksen et al., 2010; Oliva et al., 2016; Ng et al., 2018). Therefore, on their own, these inputs cannot explain why the differences between spatial selectivity in pCA1 and dCA1 observed in those studies disappear in the present study. The availability of the on-track sensory cues may increase spatial selectivity of the non-LEC inputs on the circular track compared with the other environments used in the earlier studies. Alternatively, increased complexity of the environment may increase spatial encoding demands on the hippocampal system, which may respond by recruiting dCA1 in a task dependent manner. This can be achieved by increasing responsiveness of dCA1 to preexisting spatial inputs with increasing complexity. Additional experiments are required to test whether one or both of these mechanisms contribute to increased spatial selectivity in dCA1 in the present experimental protocol compared with previous reports, including the role of LEC as the possible modulator of contributions of non-LEC inputs to the CA1 spatial code (Lu et al., 2013).

Together with the more coherent rotation of dCA1 compared with pCA1 during local-global cue conflict, the comparable spatial selectivity between pCA1 and dCA1 in this protocol shows that dCA1 has at least as robust a representation of space as pCA1, if not more. This challenges the notion that dCA1 is inherently less spatially selective than pCA1.

Deep versus superficial CA1
Superficial dCA1 receives strongest inputs from LEC and deep pCA1 receives strongest inputs from MEC (Masurkar et al., 2017). This connectivity pattern correlates with superficial versus deep segregation of path integration derived and landmark related representations (Geiller et al., 2017; Fattahi et al., 2018; Sharif et al., 2021). Correspondingly, deep versus superficial spatial selectivity differences coexist with proximodistal differences on a linear track (Oliva et al., 2016). Tetrode recordings used in this study make it impossible to pinpoint superficial versus deep location of the neurons reported here, and thus a future study will have to verify whether there is a superficial versus deep difference along with the proximodistal functional segregation reported here.

Reference frames in CA1
The hippocampus was originally proposed to create a unitary representation of absolute space (O'Keefe and Nadel, 1978). This unitary representation requires a single reference frame with a single origin with respect to which every point in space is encoded. However, several independent reference frames may coexist, and may generally agree with one another, giving an appearance of a unitary code for space. Thus, different neurons firing at a specific location may be encoding that location as different distances and directions from different origins. Some experimental conditions demonstrate existence of such coexisting reference frames in CA1. Representations of proximity to barriers (Rivard et al., 2004), goal location (Gothard et al., 1996b; Fyhn et al., 2002), distance and direction to goal (Gothard et al., 1996a; Sarel et al., 2017; Aoki et al., 2019), distance and direction to landmarks (McNaughton et al., 1995; Deshmukh and Knierim, 2013) may coexist with the classic place cells representing space in allocentric coordinates. These place fields in allocentric coordinates themselves may be formed by combining inputs from two or more boundary vector cells (O'Keefe and Burgess, 1996; Hartley et al., 2000) or grid cells (Solstad et al., 2006; de Almeida et al., 2009; Savelli and Knierim, 2010; Monaco et al., 2011), or a combination of sensory and self-generated inputs (Deshmukh and Knierim, 2013). Thus, even the classic place cells may be encoding space in different reference frames.

Creating an explicit conflict between reference frames reveals their influence on hippocampal representation of space (Gothard et al., 1996a,b; Zinyuk et al., 2000; Knierim, 2002; Lee et al., 2004). In the double rotation protocol used in this article, some regions involved in spatial encoding show coherent rotations while the others show weak to no coherence in rotation (Lee et al., 2004, 2015; Neunuebel et al., 2013; Neunuebel and Knierim, 2014; Sharma et al., 2020). The dissociation of responses to the double rotation manipulation along the proximodistal axis of CA1 shown here demonstrates that the non-unitary representation of space in the hippocampal output (via CA1) reflects strong conflict apparent in its inputs (in pCA1) or lack thereof (in dCA1). Regions of the brain differentially targeted (directly or indirectly) by pCA1 and dCA1 (Naber et al., 2001; Witter and Amaral, 2004), thus, receive spatial inputs that have differential influence of different spatial reference frames. Further studies are required to elaborate the role of this difference of spatial inputs in functioning of these target regions.

References
Aoki Y, Igata H, Ikegaya Y, Sasaki T (2019) The integration of goal-directed signals onto spatial maps of hippocampal place cells. Cell Rep 27:1516–1527.e5.

Burke SN, Maurer AP, Nematollahi S, Uprety AR, Wallace JL, Barnes CA (2011) The influence of objects on place field expression and size in distal hippocampal CA1. Hippocampus 21:783–801.

Burwell RD (2000) The parahippocampal region: corticocortical connectivity. Ann NY Acad Sci 911:25–42.

Buzsáki G, Peyrache A (2016) Jim's work pointed in the right direction. In: James B Ranck Sympposium at SUNY Downstate. https://www.youtube.com/watch?v=2da6gzF9eo0&t=24m13s

de Almeida L, Idiart M, Lisman JE (2009) The input-output transformation of the hippocampal granule cells: from grid cells to place fields. J Neurosci 29:7504–7512.

Deshmukh SS, Knierim JJ (2011) Representation of non-spatial and spatial information in the lateral entorhinal cortex. Front Behav Neurosci 5:69.

Deshmukh SS, Knierim JJ (2013) Influence of local objects on hippocampal representations: landmark vectors and memory. Hippocampus 23:253–267.

Deshmukh SS, Yoganarasimha D, Voicu H, Knierim JJ (2010) Theta modulation in the medial and the lateral entorhinal cortices. J Neurophysiol 104:994–1006.

Ding SL (2013) Comparative anatomy of the prosubiculum, subiculum, presubiculum, postsubiculum, and parasubiculum in human, monkey, and rodent. J Comp Neurol 521:4145–4162.

Dolleman-Van Der Weel MJ, Witter MP (1996) Projections from the nucleus reuniens thalami to the entorhinal cortex, hippocampal field CA1, and the subiculum in the rat arise from different populations of neurons. J Comp Neurol 364:637–650.

Dolleman-van der Weel MJ, Griffin AL, Ito HT, Shapiro ML, Witter MP, Vertes RP, Allen TA (2019) The nucleus reuniens of the thalamus sits at the nexus of a hippocampus and medial prefrontal cortex circuit enabling memory and behavior. Learn Mem 26:191–205.

Fattahi M, Sharif F, Geiller T, Royer S (2018) Differential representation of landmark and self-motion information along the CA1 radial axis: self-motion generated place fields shift toward landmarks during septal inactivation. J Neurosci 38:6766–6778.

Fox SE, Ranck JB (1981) Electrophysiological characteristics of hippocampal complex-spike cells and theta cells. Exp Brain Res 41:399–410.

Frank LM, Brown EN, Wilson MA (2001) A comparison of the firing properties of putative excitatory and inhibitory neurons from CA1 and the entorhinal cortex. J Neurophysiol 86:2029–2040.

Fyhn M, Molden S, Hollup S, Moser M-B, Moser E (2002) Hippocampal neurons responding to first-time dislocation of a target object. Neuron 35:555–566.

Geiller T, Fattahi M, Choi J-S, Royer S (2017) Place cells are more strongly tied to landmarks in deep than in superficial CA1. Nat Commun 8:14531.

Gothard KM, Skaggs WE, McNaughton BL (1996a) Dynamics of mismatch correction in the hippocampal ensemble code for space: interaction between path integration and environmental cues. J Neurosci 16:8027–8040.

Gothard KM, Skaggs WE, Moore KM, McNaughton BL (1996b) Binding of hippocampal CA1 neural activity to multiple reference frames in a landmark-based navigation task. J Neurosci 16:823–835.

Hafting T, Fyhn M, Molden S, Moser M-B, Moser EI (2005) Microstructure of a spatial map in the entorhinal cortex. Nature 436:801–806.

Hartley T, Burgess N, Lever C, Cacucci F, O'Keefe J (2000) Modeling place fields in terms of the cortical inputs to the hippocampus. Hippocampus 10:369–379.

Henriksen EJ, Colgin LL, Barnes CA, Witter MP, Moser M-B, Moser EI (2010) Spatial representation along the proximodistal axis of CA1. Neuron 68:127–137.

Holm S (1979) A simple sequentially rejective multiple test procedure. Scand J Stat 6:65–70.

Igarashi KM, Lu L, Colgin LL, Moser M-B, Moser EI (2014) Coordination of entorhinal-hippocampal ensemble activity during associative learning. Nature 510:143–147.

Ishizuka N, Weber J, Amaral DG (1990) Organization of intrahippocampal projections originating from CA3 pyramidal cells in the rat. J Comp Neurol 295:580–623.

Ito HT, Schuman EM (2012) Functional division of hippocampal area CA1 via modulatory gating of entorhinal cortical inputs. Hippocampus 22:372–387.

Jankowski MM, Islam MN, Wright NF, Vann SD, Erichsen JT, Aggleton JP, O'Mara SM (2014) Nucleus reuniens of the thalamus contains head direction cells. Elife 3:e03075.

Jankowski MM, Passecker J, Islam MN, Vann S, Erichsen JT, Aggleton JP, O'Mara SM (2015) Evidence for spatially-responsive neurons in the rostral thalamus. Front Behav Neurosci 9:256.

Knierim JJ (2002) Dynamic interactions between local surface cues, distal landmarks, and intrinsic circuitry in hippocampal place cells. J Neurosci 22:6254–6264.

Knierim JJ, Neunuebel JP, Deshmukh SS (2014) Functional correlates of the lateral and medial entorhinal cortex: objects, path integration and local-global reference frames. Philos Trans R Soc Lond B Biol Sci 369:20130369.

Kumar M, Deshmukh SS (2020) Differential propagation of ripples along the proximodistal and septotemporal axes of dorsal CA1 of rats. Hippocampus 30:970–986.

Lee I, Yoganarasimha D, Rao G, Knierim JJ (2004) Comparison of population coherence of place cells in hippocampal subfields CA1 and CA3. Nature 430:456–459.

Lee H, Wang C, Deshmukh SS, Knierim JJ (2015) Neural population evidence of functional heterogeneity along the CA3 transverse axis: pattern completion versus pattern separation. Neuron 87:1093–1105.

Leutgeb S, Ragozzino KE, Mizumori SJ (2000) Convergence of head direction and place information in the CA1 region of hippocampus. Neuroscience 100:11–19.

Lu L, Leutgeb JK, Tsao A, Henriksen EJ, Leutgeb S, Barnes CA, Witter MP, Moser M-B, Moser EI (2013) Impaired hippocampal rate coding after lesions of the lateral entorhinal cortex. Nat Neurosci 16:1085–1093.

Manns JR, Eichenbaum H (2009) A cognitive map for object memory in the hippocampus. Learn Mem 16:616–624.

Masurkar AV, Srinivas KV, Brann DH, Warren R, Lowes DC, Siegelbaum SA (2017) Medial and lateral entorhinal cortex differentially excite deep versus superficial CA1 pyramidal neurons. Cell Rep 18:148–160.

McNaughton BL, Knierim JJ, Wilson MA (1995) Vector encoding and the vestibular foundations of spatial cognition: neurophysiological and computational mechanisms. In: The cognitive neurosciences, pp 585–595. Cambridge: The MIT Press.

Monaco JD, Abbott LF, Abbott LF (2011) Modular realignment of entorhinal grid cell activity as a basis for hippocampal remapping. J Neurosci 31:9414–9425.

Naber PA, Lopes da Silva FH, Witter MP (2001) Reciprocal connections between the entorhinal cortex and hippocampal fields CA1 and the subiculum are in register with the projections from CA1 to the subiculum. Hippocampus 11:99–104.

Nakamura NH, Flasbeck V, Maingret N, Kitsukawa T, Sauvage MM (2013) Proximodistal segregation of nonspatial information in CA3: preferential recruitment of a proximal CA3-distal CA1 network in nonspatial recognition memory. J Neurosci 33:11506–11514.

Nakazawa Y, Pevzner A, Tanaka KZ, Wiltgen BJ (2016) Memory retrieval along the proximodistal axis of CA1. Hippocampus 26:1140–1148.

Neunuebel JP, Knierim JJ (2014) CA3 retrieves coherent representations from degraded input: direct evidence for CA3 pattern completion and dentate gyrus pattern separation. Neuron 81:416–427.

Neunuebel JP, Yoganarasimha D, Rao G, Knierim JJ (2013) Conflicts between local and global spatial frameworks dissociate neural representations of the lateral and medial entorhinal cortex. J Neurosci 33:9246–9258.

Ng CW, Elias GA, Asem JSA, Allen TA, Fortin NJ (2018) Nonspatial sequence coding varies along the CA1 transverse axis. Behav Brain Res 354:39–47.

O'Keefe J, Nadel L (1978) The hippocampus as a cognitive map. Oxford: Clarendon Press.

O'Keefe J, Burgess N (1996) Geometric determinants of the place fields of hippocampal neurons. Nature 381:425–428.

Oliva A, Fernández-Ruiz A, Buzsáki G, Berényi A (2016) Spatial coding and physiological properties of hippocampal neurons in the cornu ammonis subregions. Hippocampus 26:1593–1607.

Omer DB, Maimon SR, Las L, Ulanovsky N (2018) Social place-cells in the bat hippocampus. Science 359:218–224.

Ranck JB (1973) Studies on single neurons in dorsal hippocampal formation and septum in unrestrained rats. I. Behavioral correlates and firing repertoires. Exp Neurol 41:461–531.

Rivard B, Li Y, Lenck-Santini P-P, Poucet B, Muller RU (2004) Representation of objects in space by two classes of hippocampal pyramidal cells. J Gen Physiol 124:9–25.

Sarel A, Finkelstein A, Las L, Ulanovsky N (2017) Vectorial representation of spatial goals in the hippocampus of bats. Science 355:176–180.

Savelli F, Knierim JJ (2010) Hebbian analysis of the transformation of medial entorhinal grid-cell inputs to hippocampal place fields. J Neurophysiol 103:3167–3183.

Shapiro ML, Tanila H, Eichenbaum H (1997) Cues that hippocampal place cells encode: dynamic and hierarchical representation of local and distal stimuli. Hippocampus 7:624–642.

Sharif F, Tayebi B, Buzsáki G, Royer S, Fernandez-Ruiz A (2021) Subcircuits of deep and superficial CA1 place cells support efficient spatial coding across heterogeneous environments. Neuron 109:363–376.e6.

Sharma A, Nair IR, Doreswamy Y (2020) Attractor-like spatial representations in the subicular complex network. bioRxiV 935379. doi: 10.1101/2020.02.05.935379

Skaggs WE, McNaughton BL, Wilson MA, Barnes CA (1996) Theta phase precession in hippocampal neuronal populations and the compression of temporal sequences. Hippocampus 6:149–172.

Solstad T, Moser EI, Einevoll GT (2006) From grid cells to place cells: a mathematical model. Hippocampus 16:1026–1031.

Squire LR, Stark CE, Clark RE (2004) The medial temporal lobe. Annu. Rev. Neurosci 27:279–306.

Steward O, Scoville SA (1976) Cells of origin of entorhinal cortical afferents to the hippocampus and fascia dentata of the rat. J Comp Neurol 169:347–370.

Suzuki WA, Miller EK, Desimone R (1997) Object and place memory in the macaque entorhinal cortex. J Neurophysiol 78:1062–1081.

Vertes RP, Hoover WB, Do Valle AC, Sherman A, Rodriguez JJ (2006) Efferent projections of reuniens and rhomboid nuclei of the thalamus in the rat. J Comp Neurol 499:768–796.

Wang C, Chen X, Lee H, Deshmukh SS, Yoganarasimha D, Savelli F, Knierim JJ (2018) Egocentric coding of external items in the lateral entorhinal cortex. Science 362:945–949.

Witter MP, Amaral DG (2004) Hippocampal formation, Ed 3, pp 635–704. Amsterdam: Elsevier.

Xiao Z, Lin K, Fellous J-M (2020) Conjunctive reward-place coding properties of dorsal distal CA1 hippocampus cells. Biol Cybern 114:285–301.

Xu X, Sun Y, Holmes TC, López AJ (2016) Noncanonical connections between the subiculum and hippocampal CA1. J Comp Neurol 524:3666–3673.

Yoganarasimha D, Yu X, Knierim JJ (2006) Head direction cell representations maintain internal coherence during conflicting proximal and distal cue rotations: comparison with hippocampal place cells. J Neurosci 26:622–631.

Yoganarasimha D, Rao G, Knierim JJ (2011) Lateral entorhinal neurons are not spatially selective in cue-rich environments. Hippocampus 21:1363–1374.

Zinyuk L, Kubik S, Kaminsky Y, Fenton AA, Bures J (2000) Understanding hippocampal activity by using purposeful behavior: place navigation induces place cell discharge in both task-relevant and task-irrelevant spatial reference frames. Proc Natl Acad Sci USA 97:3771–3776.